Influence of the support on stabilizing local defects in strained monolayer oxide films

Shuqiu Wang, Xiao Hu, Jacek Goniakowski, Claudine Noguera, Martin R. Castell

Influence of the support on stabilizing local defects in strained monolayer oxide films

Shuqiu Wang,[a] Xiao Hu,[a] Jacek Goniakowski,[b] Claudine Noguera,[b] and Martin R. Castell[*a]

[a] Department of Materials, University of Oxford, Parks Road, Oxford, OX1 3PH, U.K.

[b] CNRS-Sorbonne Université, UMR 7588, INSP, F-75005 Paris, France

* Email: martin.castell@materials.ox.ac.uk

ABSTRACT: Two-dimensional materials with a honeycomb lattice, such as graphene and hexagonal boron nitride, often contain local defects in which the hexagonal elements are replaced by four, five, seven, and eight-membered rings. An example is the Stone-Wales (S-W) defect, where a bond rotation causes four hexagons to be transformed into a cluster of two pentagons and two heptagons. A further series of similar defects incorporating divacancies results in larger structures of non-hexagonal elements. In this paper, we use scanning tunneling microscopy (STM) and density functional theory (DFT) modeling to investigate the structure and energetics of S-W and divacancy defects in a honeycomb (2 × 2) Ti_2O_3 monolayer grown on an Au(111) substrate. The epitaxial rumpled Ti_2O_3 monolayer is pseudomorphic and in a state of elastic compression. As a consequence, divacancy defects, which induce tension in freestanding films, relieve the compression in the epitaxial Ti_2O_3 monolayer and therefore have significantly

lower energies when compared with their freestanding counterparts. We find that at the divacancy defect sites there is a local reduction of the charge transfer between the film and the substrate, the rumpling is reduced, and the film has an increased separation from the substrate. Our results demonstrate the capacity of the substrate to significantly influence the energetics, and hence favor vacancy-type defects, in compressively strained 2D materials. This approach could be applied more broadly, for example to tensile monolayers, where vacancy-type defects would be rare and interstitial-type defects might be favored.

KEYWORDS: local structural defects, elastic strain, monolayers, two-dimensional materials, ultrathin oxide films, scanning tunneling microscopy (STM), density functional theory (DFT)

1. Introduction

Two-dimensional materials of atomic thickness often have a honeycomb lattice, such as graphene and hexagonal boron nitride (h-BN).[1] These films consist of fully coordinated atoms and they interact weakly with their supporting substrates via van der Waals bonding. There are several different atomic configurations of the honeycomb lattice. Graphene consists of a flat layer of carbon atoms arranged in a simple hexagonal lattice.[2] Silicene has a buckled honeycomb structure, where the atoms are subdivided into two planes of silicon atoms.[3] Hexagonal boron nitride has a flat layer of alternating boron and nitrogen atoms, and this heteroelemental nature adds chemical and polar complexity to the system.[4] Bilayer silica consists of two layers of tetrahedral structural units in which four oxygen atoms surround a silicon atom.[5] Crystalline monolayers of water (ice) can form a H-bonded puckered honeycomb network.[6]

2D materials with a honeycomb structure often contain local structural defects where the hexagons are replaced by 4, 5, 7 and 8-membered rings. The non-hexagons can be generated through Stone-Wales (S-W) transformations. This mechanism was first predicted in graphene and involves rotating a C-C dimer by 90° to transform four hexagons into two pentagons and two heptagons.[7] A further series of related defects incorporating divacancies (DV) results in larger structures of non-hexagonal elements. The simplest divacancy defect consists of one octagon and two pentagons and is called a DV(5-8-5) defect which is named after the ring sizes of the building blocks. Other structures include the DV(555-777) defect, containing three pentagons and three heptagons, and the DV(5555-6-7777) defect, containing four pentagons and four heptagons surrounding a hexagon.[8] These structures have been widely investigated in graphene,[9,10] h-BN,[11] transition metal dichalcogenides,[12] bilayer silica[13] and ice monolayers.[14,15] Generally, these defects have relatively high formation energies (e.g. 5-8 eV in graphene)[16] mainly due to the bond distortions in the non-hexagonal rings. Small 4 and 5-membered rings result in bond compression, whereas large 7 and 8-membered rings result in bond expansion. The strain resulting from 5 and 7-membered rings is lower than for 4 and 8-membered rings.[17] 5 and 7-membered rings often form defect pairs that have relatively low strain energy. In graphene, both DV(5-8-5) and DV(555-777) defects have two missing carbon atoms but the latter, although it is larger, has a lower formation energy due to smaller bond distortions.

Mechanically straining the graphene lattice results in a change in the formation energies of the S-W defect and the DV(5-8-5) defect.[18,19] An alternative approach to investigate the influence of lattice strain on the defects is to grow the 2D material via epitaxial growth on lattice-mismatched or patterned substrates.[20–22] This results in compression or tension of the supported film and has been reported in graphene supported on a Ni(111) substrate,[22] where the small lattice mismatch

between graphene and Ni(111) allows the carbon hexagons to be in registry with the substrate. However, the Ni(111) substrate barely influences the behavior of the defects because the energy gain from the interfacial van der Waals interaction (0.7 eV per two carbon atoms)[23] is negligible compared with the high energy cost of distorting the C-C bonds (5-8 eV).[16] What is required then to investigate the effects of lattice strain, is a system where the energy gain from adhesion due to epitaxy is sufficiently high to compensate for the elastic energy loss due to film distortion. An example of such a system, a Ti_2O_3 epitaxial monolayer on an Au(111) substrate, is investigated in this paper. Ti_2O_3 monolayers have a (2 × 2) honeycomb structure that is geometrically similar to that of graphene.[24,25] The oxide film is stabilized by the structural registry with, and the charge transfer to, the substrate, which results in a substantial adhesion energy.

Using Ti_2O_3 monolayers supported on Au(111), we explore the role of epitaxial strain in determining the structural and electronic properties of local structural defects. Previous work has revealed the presence of non-hexagonal defects in monolayer films of Ti_2O_3 on Pt(111), V_2O_3 on Pd(111)[24,26] and Cu_2O on Cu(111).[27] In our study, a series of defects with different arrangements of polygons were observed in the Ti_2O_3 honeycomb structure. Their atomic structures, electronic properties and defect energies are determined by combining scanning tunneling microscopy (STM) and density functional theory (DFT). Despite the differences in the nature of the chemical bonding, we find that the metal-oxygen-metal bonds structurally evolve in a similar way to those of graphene. The physical origin of the defects is the same, i.e. they incorporate non-hexagonal rings at the expense of strain energy. Our study demonstrates that the compressive strain in the oxide film due to the Au(111) support barely affects the S-W defect, whereas it significantly reduces the energies of the divacancy defects. In addition, STM which was previously used to observe strain fields in graphene around single vacancies,[28] domain boundaries,[29] and

nanobubbles,[30] as well as in graphene–black phosphorus heterostructures[31] here reveals the existence of an anisotropic strain field surrounding the DV(555-777) defect as a result of small atomic height displacements. Finally, we also observe a so-called 'flower' defect consisting of six pentagon-heptagon pairs around a core of seven hexagons.

2. Methods

2.1 Experimental methods

The experiments were performed in an ultrahigh vacuum (UHV) system at a base pressure of 10^{-8} Pa. STM measurements were carried out in a JEOL instrument (JSTM 4500XT) at room temperature using etched tungsten tips in constant current mode. The Ti_2O_3 honeycomb ultrathin films on Au(111) substrates were grown according to the description detailed in Ref.[25]. Mica-supported Au(111) single crystals (Agilent Technologies, U.K.) were used as substrates. Au(111) substrates were sputtered by Ar^+ ions and UHV annealed to 600 °C for 1.5 h resulting in the herringbone reconstruction. Ti vapor is deposited using an e-beam evaporator (Oxford Applied Research EGN4) from a 99.99% pure Ti rod supplied by Goodfellow, U.K. The surfaces are then annealed in 10^{-6} Pa O_2 for 0.5 h to create the (2 × 2) Ti_2O_3 honeycomb ultrathin films. Most STM images presented in the paper are the results of multiple frame averaging (MFA) using a software package called Smart Align with the general method described in Ref.[32] and the specific application to STM described in Ref.[33]. Quantitative processing methods are provided in the Supporting Information. The STM images were smoothed using ImageJ packages.

2.2 Theoretical Calculations

All computational results were obtained within a plane wave density functional approach, with a spin-polarized gradient-corrected PW91 exchange-correlation functional,[34] and the projector

augmented wave method[35] implemented in VASP.[36,37] Simulated STM images were obtained within the Tersoff–Hamann approximation[38] at a positive bias of $E - E_F = +2\,V$ and the LDOS was plotted at 5.2 Å from the center of the first Au substrate plane. Atomic charges were estimated according to Bader's prescription.[39,40]

The formation energies of defects in Au-supported Ti_2O_3 films were evaluated with respect to the pristine supported honeycomb film, E_{form} = E(Ti_2O_3 + defect/Au) – E(Ti_2O_3/Au) + n/m[E(Ti_2O_3 /Au) – E(Au)], where E(Ti_2O_3 +defect/Au) and E(Ti_2O_3/Au) are the total energies of the defective and pristine supported honeycomb films, respectively, and the factor n/m accounts for the Ti_2O_3 deficiency in the defective film (n =1 formula unit in all considered cases, except for the Stone-Wales defect for which n = 0), with respect to the number of oxide formula units in the surface unit cell (m = 24). Further details can be found in Supporting Information.

3. Results & discussion

3.1 The pristine Ti_2O_3 (2 × 2) honeycomb structure.

The structural model of the titanium oxide monolayer epitaxial film on Au(111) is shown in Fig. 1a. The film has Ti_2O_3 stoichiometry and a honeycomb structure. The film adopts the 2 × 2 periodicity of the Au(111) substrate with the Ti atoms located in Au(111) three-fold hollow sites and the O atoms located in on-top positions.[25,41] A Ti_2O_3 (2 × 2) unit cell is highlighted in Fig. 1a. DFT calculations show that the films incorporate substantial rumpling with the O atoms shifted away from the substrate with respect to the Ti atoms by 0.7 Å, as shown in Fig. 1b(i). Despite the O atoms being closest to the STM tip during scanning, typical empty states STM images show the Ti locations as bright spots in the images (Fig. 1c). A calculated STM image in

the bottom right corner of Fig. 1c demonstrates good correspondence between theory and experiment for this system.

DFT calculations for the Ti_2O_3 monolayer were also carried out on a hypothetical freestanding film. These simulations result in a flat film with a lattice parameter of 6.35 Å, as shown in Fig. 1b(ii). The rumpling of the supported film is due to the effect of electron transfer from the film to the electronegative Au substrate. This causes Coulomb interactions to push the O anions away from the substrate, and attract the Ti cations towards the substrate.[42,43] The resulting equilibrium in-plane lattice parameter of the Au-supported honeycomb film can be estimated to be about 5.9 Å (see Supplementary Information S2f). This value is much smaller than that of the unsupported film, but somewhat larger than the (2 × 2)-Au(111) periodicity of 5.77 Å. This indicates that the pseudomorphic Ti_2O_3 film is in a state of in-plane elastic compression.

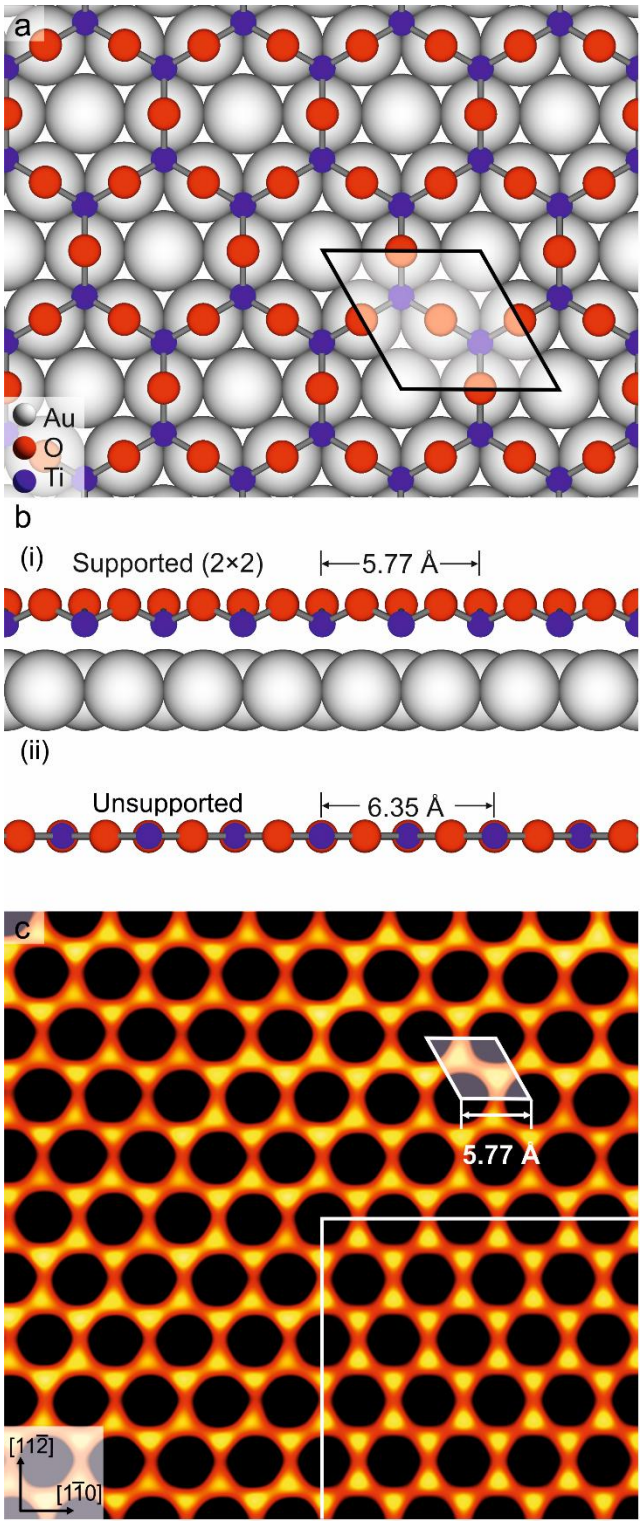

Fig. 1 Pristine Ti_2O_3 (2 × 2) honeycomb structure. (a) A schematic of the Ti_2O_3 monolayer with a honeycomb lattice on Au(111). Ti atoms (blue) are located in Au(111) (grey) three-fold hollow sites, and O atoms (red) are located in on-top positions. A Ti_2O_3 2 × 2 unit cell is highlighted. Side views of the calculated structures of supported (i) and freestanding (ii) Ti_2O_3

films. (c) Experimental STM image of the pristine film with a 2 × 2 Ti_2O_3 unit cell highlighted. The atomically resolved (2 × 2) honeycomb lattice with a periodicity of 5.77 Å serves as a calibration lattice for the experimental STM images. The STM image is averaged from 88 raw frames to enhance the signal-to-noise ratio, details described in the Supporting Information (image width 5.2 nm, V_s = 0.9-1.0 V and I_t = 0.22-0.24 nA). The inset shows a DFT simulation of the STM image ($E - E_F = +2\ V$, distance from the center of the first Au substrate plane is 5.2 Å).

3.2 Visualization of defects.

The relationship between the Stone-Wales (S-W), DV(5-8-5), DV(555-777) and DV(5555-6-7777) defects can be represented through the S-W transformation in combination with a divacancy (DV) formation, as illustrated in Fig. 2. The first row in Fig. 2 shows the initial structure in each case. The atoms in motion are highlighted throughout the process to help visualize the bond rotation. The middle row qualitatively shows the movement in each case. The final optimized structures are shown in the bottom row where 5, 6, 7 and 8-membered rings are clustered in various arrangements.

The first column in Fig. 2 shows the formation of a S-W defect. A Ti_2O unit (Fig. 2a) can be thought to undergo a bond rotation of 90° to form a S-W defect where four hexagons are replaced by two pentagons and two heptagons (Fig. 2i). The second column in Fig. 2 shows the formation of a DV(5-8-5) defect. The Ti_2O_3 cluster highlighted in Fig. 2b is removed. The resultant four dangling bonds (Fig. 2f) recombine to form two pentagons and one octagon. The coordination of the Ti and O atoms is maintained for this, and indeed for all the defects, as is the Ti_2O_3 stoichiometry. The Ti_2O_3 vacancy here is called a "divacancy" because it incorporates two missing Ti atoms, and from a structural point of view this is analogous to two missing carbon atoms in graphene. The DV(5-8-5) defect can transform into a DV(555-777) defect via a S-W transformation, as shown in the third column in Fig. 2. A Ti_2O unit shared amongst an octagon and three hexagons (Fig. 2c) undergoes a 90° rotation to form a DV(555-777) defect (Fig. 2k).

The DV(555-777) defect contains three pairs of alternating 5 and 7-membered rings. Following the same mechanism, the DV(555-777) defect undergoes a S-W rotation and results in a loop of four pentagon-heptagon pairs surrounding a hexagon, as shown in the right-hand column of Fig. 2. This structure is called the DV(5555-6-7777) defect.

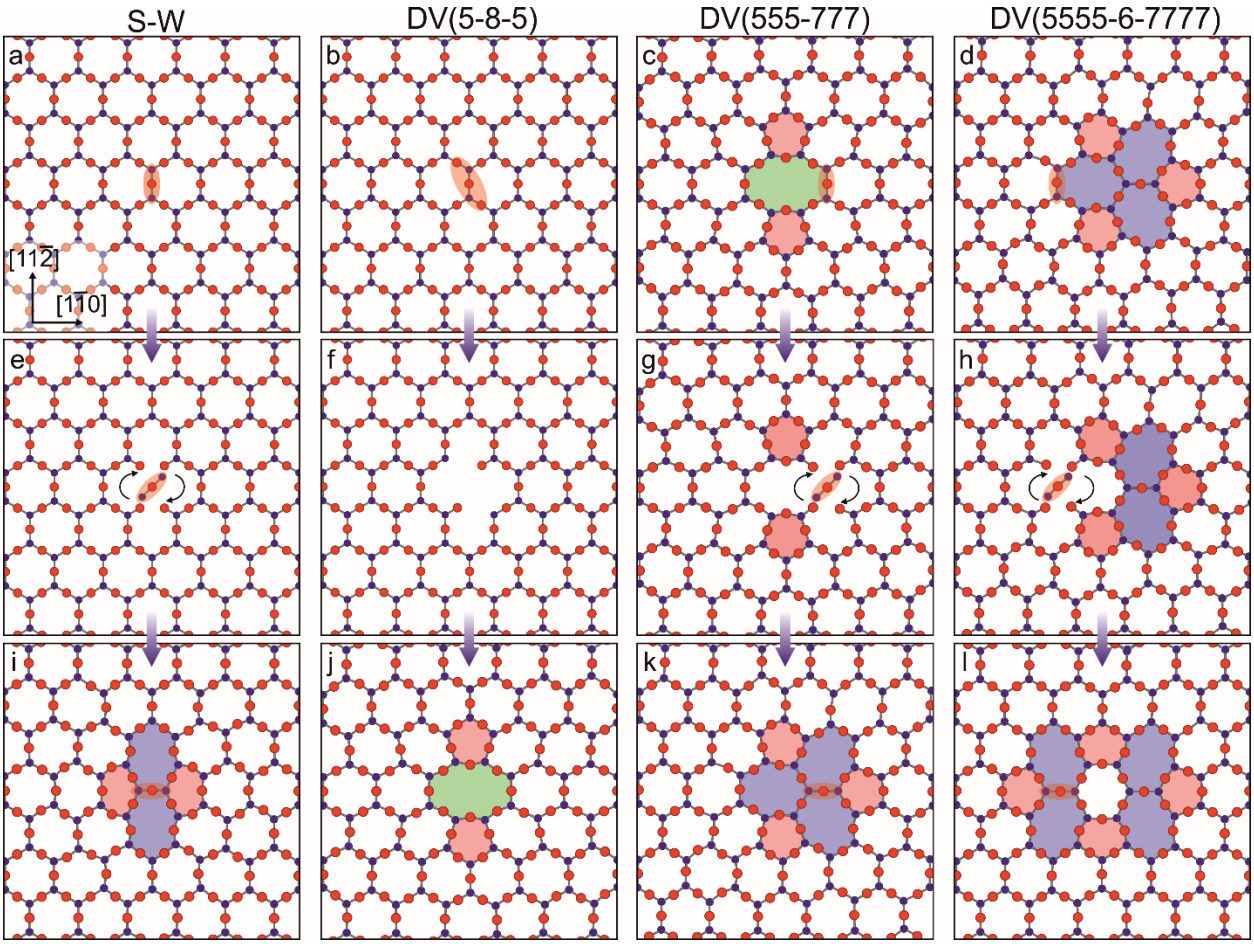

Fig. 2 Schematic representation of the relationship of the Stone-Wales (S-W), DV(5-8-5), DV(555-777) and DV(5555-6-7777) defects. The initial structures are shown in (a-d), in which the atoms that move are indicated by an oval. The movements in each case are qualitatively shown in (e-h), where the rotation is indicated by black arrows. The final optimized structures are shown in (i-l). The pentagons, heptagons and octagons are highlighted in pink, blue and green. Ti and O atoms are blue and red balls, respectively. The Au substrate atoms are not shown.

The schematic models in Fig. 2 illustrate that the existence and evolution of the S-W and DV defects are linked to the capability of bonds to break and of a Ti_2O unit to undergo a rotation to

allow new bonding configurations to form. To analyze the typical energies involved in these transitions we calculated the energetics of rotation of a Ti_2O unit that results in the formation of a S-W defect, as shown in Fig. 3. This figure shows that there are two possible intermediate atomic arrangements (Fig.3 b and c). In Fig. 3b there are two dangling oxygen atoms and this state has an energy of 5.3 eV with respect to the pristine lattice shown in Fig. 3a. This atomic configuration is similar to that calculated for unsupported graphene [44] or unsupported h-BN monolayer.[45] The alternative configuration shown in Fig. 3c only has one dangling oxygen atom, has a lower calculated energy of 3.6 eV, and is similar to the transition state of Ni-supported graphene [46] and unsupported silicene.[47]

For completeness, we have also calculated the energies of the configurations shown in Fig. 3b,c for an unsupported HC monolayer (6 eV, 3.2 eV, respectively), and these are not significantly different from the supported situation. The energy of the intermediate atomic arrangements can be linked to the number of dangling oxygen atoms which is why the configuration in Fig.3b has approximately twice the energy of that in Fig. 3c. These dangling oxygen energies are consistent with values of the cohesive energy per bond in bulk Ti_2O_3 or TiO_2 which is of the order of 3 eV.[48,49] For comparison, the energy involved in a S-W bond rotation is 10.4 eV for unsupported h-BN,[45] 2.64 eV for silicene [47] and 9.2 eV for unsupported graphene.[44]

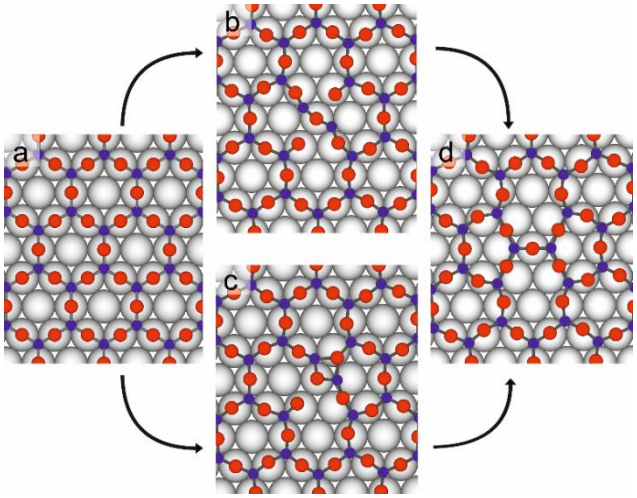

Fig. 3 Calculated reaction pathways for the creation of a S-W defect in a Ti_2O_3 honeycomb monolayer on Au(111). The relaxed geometries for the two intermediate states with (b) two or (c) one dangling oxygens shown. Ti, O and Au atoms are blue, red and grey, respectively.

In the experiments there are three mechanisms that give rise to S-W and DV defects in the Ti_2O_3 honeycomb films. The first mechanism is incorporation of defects during crystal growth or when two separately nucleated domains meet. The second is coalescence of atomic vacancies, where in our case, a cluster of two Ti and three O vacancies agglomerate to form a DV defect. The third mechanism relates to the use of STM. We have observed on a small number of occasions that during scanning tip-surface interactions can give rise to DV defects and S-W rotations. Presumably this occurs when the tip makes contact with the honeycomb film and some of the monolayer atoms are transferred onto the STM tip. We discuss this observation further in Supporting Information S4.

3.3 Defect structures in the Ti_2O_3 honeycomb monolayer.

Experimental STM observations of the defect structures are presented in the top row of Fig. 4. The main feature in the images is the clustering of polygons embedded in the honeycomb lattice. The geometry of the clusters is the same as in the models in the bottom row of Fig. 2, hence the

structures are referred to as S-W, DV(5-8-5), DV(555-777) and DV(5555-6-7777) defects. Atomic models, including the Au substrate atoms, are shown in the third row of Fig. 4. Image simulations (the second row of Fig. 4) calculated from these atomic models are in good agreement with the experimental STM images. The only visible difference is the bright region to the left of the DV(5-8-5) defect in the experimental image (Fig. 4b), probably due to contamination.

The bottom row of Fig. 4 shows the calculated variations of the Ti-O bond lengths which illustrate the strain within the structures. The bonds are colored according to an increase (red and yellow), decrease (blue), or negligible variation (green) in the bond length with respect to 1.82 Å, the value found in the pristine supported layer. In the S-W defect, the bond expansion is relatively weak and only the central Ti-O bonds are slightly compressed (Fig. 4m and Supplementary Information S3). Conversely in the divacancy defects, the Ti-O bonds are considerably expanded because the surrounding film is stretched to fill in some of the area due to the missing Ti_2O_3 unit. The DV(5-8-5) defect has twelve of the most elongated Ti-O bonds (1.85 Å, colored in red in Fig. 4n), indicating that bond expansion is localized in the octagon. The DV(555-777) defect has six significantly expanded bonds (1.85 Å, colored in red) and several moderately expanded bonds (1.82-1.84 Å, in yellow and orange). When compared with the DV(5-8-5) defect, the DV(555-777) defect is larger, but its lattice distortions are smaller and not concentrated in the central ring. The structural characteristics of the DV(555-777) and DV(5555-6-7777) defects are similar, except that the latter involves more distorted bonds.

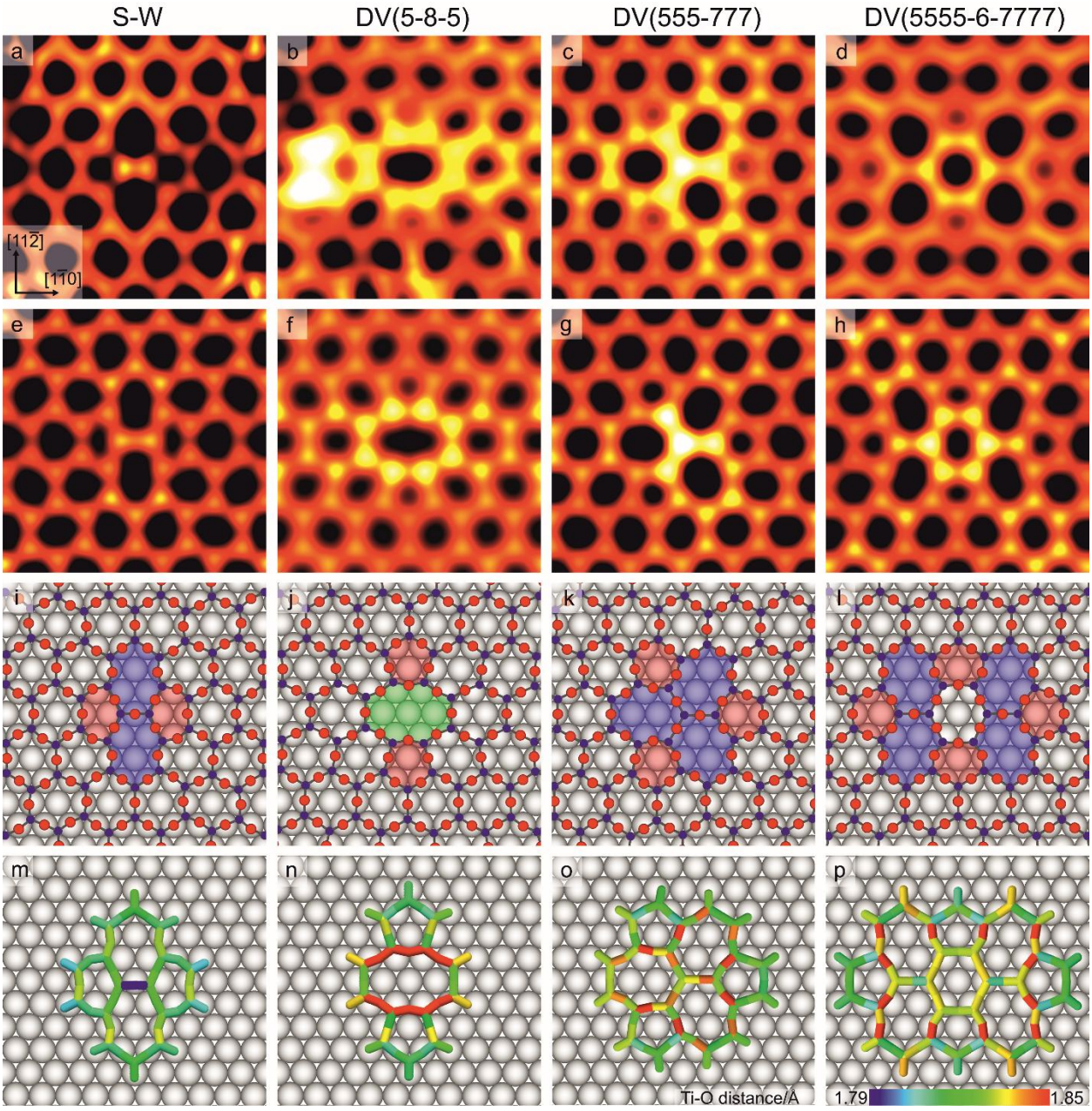

Fig. 4 Defect structures in Ti_2O_3 honeycomb. Experimental STM data (a-d), and corresponding DFT simulations (e-h) of S-W, DV(5-8-5), DV(555-777) and DV(5555-6-7777) defects. The atomic models including the Au(111) substrate atoms are shown in (i-l) with Ti atoms in blue, O atoms in red and Au atoms in grey. The STM images from (a), (c) & (d) are generated from 4, 138 and 4 frames using multiple frame averaging (MFA). The experimental STM parameters of (a-d) are V_s = 0.95 V and I_t = 0.22 nA; V_s = 0.9 V and I_t = 0.22 nA; V_s = 1.0 V and I_t = 0.2 nA; V_s = 0.9 V and I_t = 0.22 nA, respectively, with image widths of 2.9-3.0 nm for all cases. Panels (m-p) show variations of bond lengths for the defects. The bonds are colored according to an increase (red and yellow) or decrease (blue) of the bond length.

Analogous defect structures to the ones shown in Fig. 4 were also calculated for hypothetical freestanding Ti_2O_3 films. The bond distortions in the freestanding films are much larger than in the supported films. The presence of a solid substrate diminishes the degree of distortion suffered by the defective layers because the in-plane Ti-O bond stretching can be accommodated by a reduction of film rumpling.

The calculated defect formation energies in the supported Ti_2O_3 film are reported in Table 1 and range between 0.3 eV and 1.4 eV. Interestingly, these energies are significantly lower than those of similar defects in other honeycomb monolayers, e.g., graphene (5-7.6 eV),[16] h-BN (8.7-19.7 eV),[11] or bilayer silica (2.8-9 eV).[50] Moreover, their relative stability is different. Remarkably, the formation energy of the Ti_2O_3 DV(555-777) defect is considerably lower than that of the S-W defect, whereas the DV(5555-6-7777) and S-W defects are essentially isoenergetic. This finding stands in stark contrast to the usual hierarchy in other monolayers with a honeycomb structure, where S-W defects are by far systematically favored over the various divacancy defects.

Table 1. Calculated formation energies (in eV) for local structural defects in supported and freestanding Ti_2O_3 films, compared with literature values for freestanding layers of graphene, silicene, h-BN and bilayer SiO_2.

Defect	**Supported Ti_2O_3**	**Freestanding Ti_2O_3**	**Graphene**[16]	**Silicene**[47]	**h-BN**[11]	**Bilayer SiO_2**[50]
S-W	1.1	1.1	5.0	2.1	8.7	2.8
DV(5-8-5)	1.4	5.9	7.6	3.7	19.7	9.0
DV(555-777)	0.3	4.4	6.7	2.8	-	5.7
DV(5555-6-7777)	1.0	5.2	7.2	-	-	4.8

In the following discussion, we thoroughly investigate the origin of this unusual behavior and specifically analyze the role of the Au substrate. To clarify the support effect, we start by considering defects in a calculated hypothetical freestanding honeycomb Ti_2O_3 film. A perfectly flat structure is favored in an unconstrained film shown in Fig. 1b(ii), with an in-plane lattice parameter of 6.35 Å, which is much larger than that of the (2 × 2)-Au(111) substrate (5.77 Å). The calculated energies of the defects in the freestanding film are reported in Table 1. The hierarchy of the formation energies is analogous to those in graphene and in most other 2D materials. Because in calculations of defect energies the overall number of Ti-O bonds is preserved (see Supporting Information S2d), the defect energetics are therefore mainly driven by the degree of bond distortion. In the S-W defect in the freestanding monolayer, the Ti-O bonds are slightly contracted with an elastic energy cost of 0.2 eV. However in the divacancy defects, the Ti-O bonds are considerably elongated with energy costs of +3.5, +4.0, and +4.5 eV for DV(555-777), DV(5555-6-7777), and DV(5-8-5) defects, respectively. These elastic contributions account for the main part of the defect formation energies (second column in Table 1) and provide a good estimate of the relative stability of divacancy defects in the freestanding film: S-W << DV(555-777) < DV(5555-6-7777) < DV(5-8-5). More generally, this conclusion also applies to defect formation in other freestanding films.

As discussed previously, to achieve a 2 × 2 pseudomorphic structure with the Au(111) surface, the Ti_2O_3 monolayer is in a state of in-plane compressive strain of the order of 2%. It is this substrate-induced strain that is responsible for the drastically different divacancy defect energies compared with the freestanding case. The removal of a Ti_2O_3 unit in the divacancy defects results in a large tensile strain in the freestanding film, while, in the supported film, it results in a release of the compressive strain. Consequently, the elastic contribution to the defect energy

changes from large and positive (of the order of +4.0 eV) in the freestanding film, to small and negative (of the order of -0.5 eV) in the supported film. This qualitatively different elastic response of supported and freestanding films to the defect creation is the main reason for the substantially different defect energies. In particular, it explains that the energies of the S-W defects in supported and unsupported Ti_2O_3 films are similar because S-W defects only induce a small film distortion and are barely influenced by the external strain. However, the divacancy defects have lower energies in supported films because they introduce a large amount of lattice distortions and release the compressive strain. Interestingly, in the latter, the optimal arrangement of adjacent 5 and 7 member rings in the DV(555-777) defect produces the smallest strain in the freestanding films and the most efficient compressive strain release in the supported case, leading to the lowest defect energy. More generally, film structures that are buckled due to their interaction with a substrate may more readily accommodate elastic distortions produced upon defect formation, which in turn may lead to relatively low defect energies. This is clearly the case in our Au-supported honeycomb-Ti_2O_3 films but is likely also to be the case in silicene.

STM experiments provide additional information that cannot readily be modeled using *ab initio* methods due to the large number of atoms involved. After image processing using multiple frame averaging (MFA), the STM image (Fig. 5a), averaged over 138 frames without other image filtering (detailed procedures described in the Supporting Information S1), reveals an anisotropic strain field surrounding the DV(555-777) defect, a feature which is not visible in single images. The three rows of hexagons adjacent to each heptagon are marginally brighter than the other lattice atoms. The elevation of the Ti atoms extends several unit cells beyond the divacancy defect. The brightness of the Ti atoms decreases with the increase of their distance from the defect core. In particular, measurements between the first and second pairs of Ti atoms

adjacent to the heptagon show an average height difference of 0.83 ± 0.19 pm (Fig. 5b). It demonstrates the power of MFA in that it allows STM to resolve surface features into the sub-picometer regime.

The origin of the anisotropic strain field in Fig. 4a can be explained in terms of atomic displacements. The Ti atoms in the defect cores move away from their three-fold hollow adsorption sites in order to optimize the bonding. These displacements increase their elevation and their associated local density of states (LDOS) resulting in brighter spots in the STM images. These bright spots are mainly located along the heptagon directions, implying that there are greater lattice distortions adjacent to the heptagons. Similar anisotropic strain fields of a DV(555-777) defect have been theoretically predicted in 2D silica and graphene.[50,51]

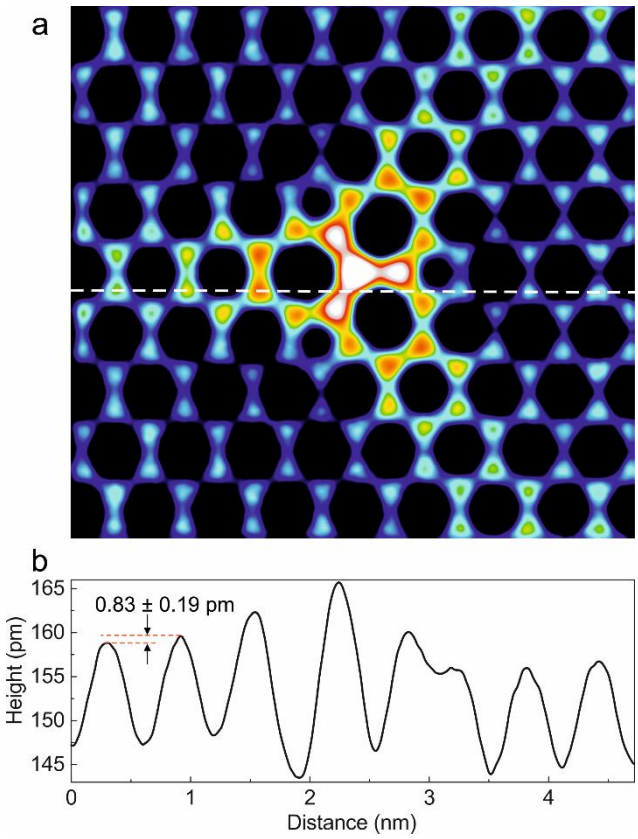

Fig. 5 Atomic structure of the strain field around a DV(555-777) defect. (a) STM image using a look-up table that has been chosen for maximum contrast. The STM image is averaged from 138 frames (image width 4.7 nm, V_s = 1.0 V and I_t = 0.2 nA). (b) Height profile along the

dashed white line shown in (a) showing the 0.83 pm height difference between the first and second pairs of Ti atoms adjacent to the heptagon. The height difference is measured from six pairs of Ti atoms.

We have also observed a defect loop of six alternating pentagons and heptagons (Fig. 6a), previously called a 'flower' defect in graphene and 2D silica.[13,52] The defect core is a crystalline domain of seven hexagons rotated by 30° with respect to the pristine honeycomb lattice. A model atomic structure is shown in Fig. 6b. The defect conserves the number of Ti and O atoms relative to the pristine lattice and maintains Ti_2O_3 stoichiometry. The Ti atoms in the rotated central domain are moved to the top sites and the O atoms are moved to bridge sites. Elevation of these Ti atoms leads to increased brightness in the defect core atoms in the STM image (Fig. 6a).

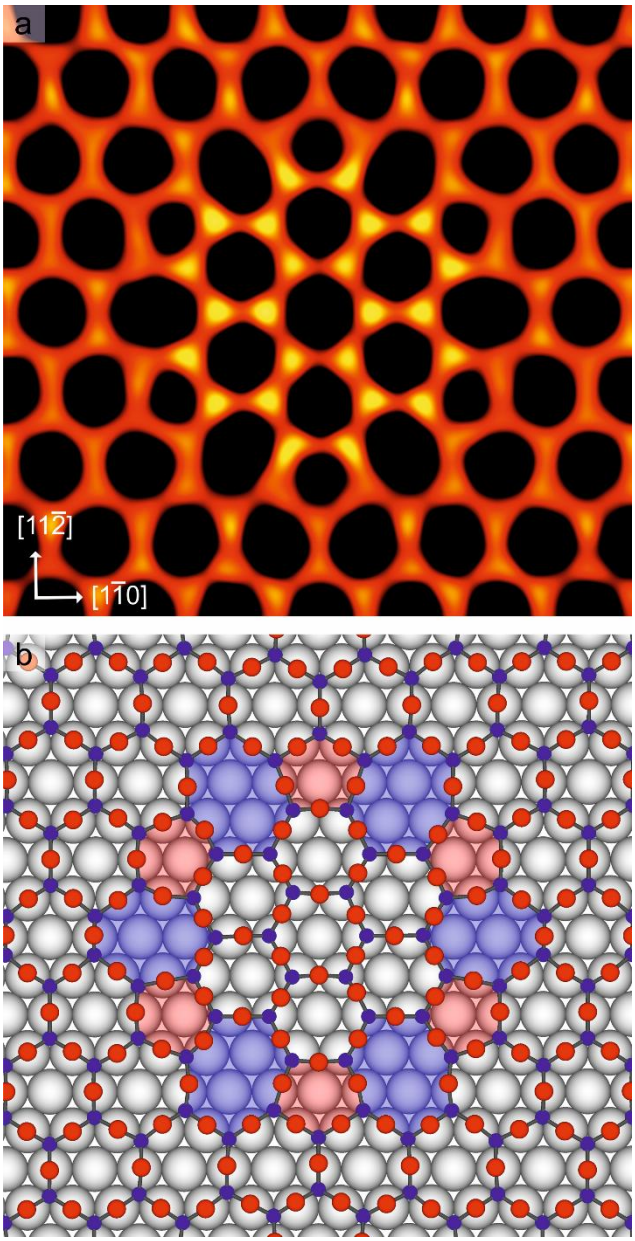

Fig. 6 'Flower' defect consisting of six pentagon-heptagon pairs. (a) STM image averaged from 12 frames (image width 4.0 nm, V_s = 0.9 V, I_t = 0.22 nA) and (b) an atomic model schematic of the 'flower' defect.

3.4 Electronic structure of the defects

The in-plane atomic displacement of the Ti atoms in the defects alters their atomic positions with respect to the Au substrate and hence the ion-Au distances. In the divacancy defects, several Ti

atoms (orange or yellow balls in Fig. 7a-d) shift away from the Au-hollow sites to bridge and top sites. This displacement increases the Ti elevation with respect to the Au surface.

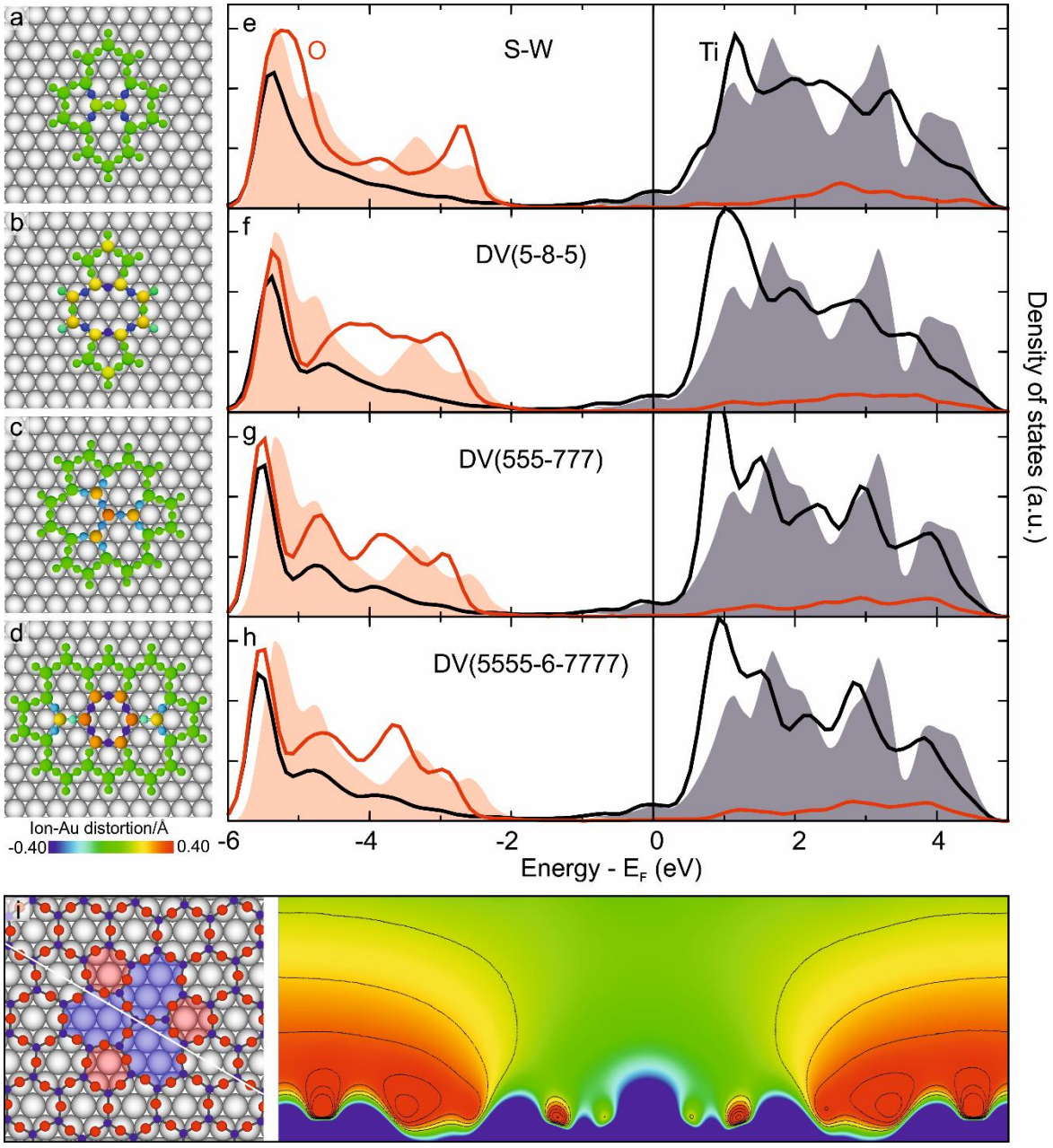

Fig. 7 Electronic structures for the defects. (a-d) Variations of ion-Au separation of the defects with respect to the pristine film. Red, green and blue denote increased, barely affected and shortened distances, respectively. (e-h) The density of states projected on Ti (black lines) and O (red lines) atoms in the defect cores. Projections on atoms in the pristine honeycomb film are indicated in shadow as a reference. (i) Map of the electrostatic potential taken through a DV(555-777) defect along the white line shown on the left. Low and high potential regions are colored in green and red, respectively. Red maxima indicate the positions of O atoms.

In the divacancy defects, the Ti displacement away from the three-fold hollow sites alters the Ti_2O_3 band alignment. Shifting Ti atoms to the Au-top sites leads to an enhanced Ti contribution to the conduction band (CB) minimum, a downshift of the CB edges and a narrowing of the Ti d-Au hybridization band. The geometrical elevation and the increased electronic signature of Ti atoms enhance the brightness of Ti atoms at the defect core in the STM images (Fig. 4a-d). In contrast to the divacancy defects, the change in the ion-Au bonding and its effect on the LDOS are negligible in the S-W defect.

Fig. 7i shows a map of the electrostatic potential through the DV(555-777) defect. The lower electrostatic potential in the center of the image corresponds to a decrease of the work function (Φ) with respect to the supported pristine oxide film. Three main dipoles contribute to the change of the gold work function when supporting the pristine film.[42,53,54] The first is due to a reduction of the dipole originating from the surface Au electrons, resulting in a compression of the Au electron distribution, which reduces Φ. The second dipole is due to charge transfer of 0.94 e^-/Ti_2O_3 from the film to the substrate, which also reduces Φ. The third dipole is due to film rumpling, which increases Φ. This rumpling dipole is dominant and results in an overall increase of Φ of 0.4 eV relative to the bare Au(111) surface. At the divacancy defect sites, Φ is reduced by 0.3 eV, mainly because of the reduced degree of rumpling at the divacancy defects (See Supplementary Information S3). This effect is visualized as a lowering of the electrostatic potential, as seen in Fig. 7i.

4. Conclusions

We have used STM to observe a series of local structural defects in the Ti_2O_3 honeycomb layer on Au(111). DFT simulations have further determined in detail the atomic and electronic

structures of the S-W and divacancy defects as well as their formation energetics. Whilst these defects are topologically similar to their counterparts in graphene and other 2D honeycomb materials, the relatively strong interaction of the oxide monolayer with the Au substrate significantly affects the defect energies and hierarchy. Moreover, we show that the elastically compressed monolayer film favors the formation of divacancy-type defects because they facilitate the release of the compressive strain. These results broaden the perspective under which such defects may be considered in other 2D materials, such as graphene or h-BN films, and open the door to new ideas in relation to the design of defect structures through a judicious combination of monolayer film and substrate. It is further probable that in monolayer films in a state of elastic tension, it will be difficult to form vacancy-type defects whereas other defects of the interstitial-type may be favored to release the tensile strain. Our study provides a solid atomic and electronic structure-based understanding of the peculiarities of local structural defects in supported ultrathin oxide films and is the starting point for further investigations into more complex defects in 2D oxide nanostructures. The defect cores with increased Ti brightness in the STM images were shown to correlate with a downshifted Ti d-Au hybridization band that will influence their chemical reactivity, for example by decreasing the CO binding energy.[55] Furthermore, enhancement of the signal-to-noise ratio of STM images using MFA provides a better comparison between experiments and simulations and reveals fine surface features that hitherto were buried in noise.

Conflicts of interest

There are no conflicts to declare.

Acknowledgements

We thank Chris Spencer (JEOL UK) for valuable technical support. S.W. acknowledges Prof. Lewys Jones for his support with the SmartAlign software package (Trinity College Dublin). S.W. acknowledges Prof. Lewys Jones and S. Ghazi Sarwat (University of Oxford) for help in proofreading the manuscript.

Abbreviations

STM, scanning tunneling microscopy/microscope; DFT, density functional theory; S-W, Stone-Wales defect; DV(5-8-5), divacancy defect of one octagon and two pentagons; DV(555-777), divacancy defect of three pentagon-heptagon pairs; DV(5555-6-7777), divacancy defect of four pentagon-heptagon pairs; h-BN, hexagonal boron nitride; MFA, multiple frame averaging; Φ, work function; LDOS, local density of states; UHV, ultrahigh vacuum.

References & notes

1 K. S. Novoselov, A. Mishchenko, A. Carvalho and A. H. Castro Neto, *Science*, 2016, **353**, 9439.

2 K. S. Novoselov, A. K. Geim, S. V. Morozov, D. Jiang, Y. Zhang, S. V. Dubonos, I. V. Grigorieva and A. A. Firsov, *Science*, 2004, **306**, 666–669.

3 P. Vogt, P. De Padova, C. Quaresima, J. Avila, E. Frantzeskakis, M. C. Asensio, A. Resta, B. Ealet and G. Le Lay, *Phys. Rev. Lett.*, 2012, **108**, 155501.

4 Y. Liu, X. Zou and B. I. Yakobson, *ACS Nano*, 2012, **6**, 7053–7058.

5 D. Löffler, J. J. Uhlrich, M. Baron, B. Yang, X. Yu, L. Lichtenstein, L. Heinke, C. Büchner, M. Heyde, S. Shaikhutdinov, H. J. Freund, R. Włodarczyk, M. Sierka and J. Sauer, *Phys. Rev. Lett.*, 2010, **105**, 146104.

6 J. Carrasco, A. Hodgson and A. Michaelides, *Nat. Mater.*, 2012, **11**, 667–674.

7 A. J. Stone and D. J. Wales, *Chem. Phys. Lett.*, 1986, **128**, 501–503.

8 G. Do Lee, C. Z. Wang, E. Yoon, N. M. Hwang, D. Y. Kim and K. M. Ho, *Phys. Rev. Lett.*, 2005, **95**, 205501.

9 J. Kotakoski, A. V. Krasheninnikov, U. Kaiser and J. C. Meyer, *Phys. Rev. Lett.*, 2011, **106**, 105505.

10 Q. Chen, A. W. Robertson, K. He, C. Gong, E. Yoon, G. Do Lee and J. H. Warner, *ACS Nano*, 2015, **9**, 8599–8608.

11 G. J. Slotman and A. Fasolino, *J. Phys.: Condens. Matter*, 2013, **25**, 045009.

12 Y.-C. Lin, T. Björkman, H.-P. Komsa, P.-Y. Teng, C.-H. Yeh, F.-S. Huang, K.-H. Lin, J. Jadczak, Y.-S. Huang, P.-W. Chiu, A. V. Krasheninnikov and K. Suenaga, *Nat. Commun.*, 2015, **6**, 6736.

13 K. M. Burson, C. Büchner, M. Heyde and H.-J. Freund, *J. Phys.: Condens. Matter*, 2017, **29**, 035002.

14 S. Nie, P. J. Feibelman, N. C. Bartelt and K. Thürmer, *Phys. Rev. Lett.*, 2010, **105**, 026102.

15 S. Maier, B. A. J. Lechner, G. A. Somorjai and M. Salmeron, *J. Am. Chem. Soc.*, 2016,

138, 3145–3151.

16 F. Banhart, J. Kotakoski and A. V. Krasheninnikov, *ACS Nano*, 2011, **5**, 26–41.

17 S. Whitelam, I. Tamblyn, T. K. Haxton, M. B. Wieland, N. R. Champness, J. P. Garrahan and P. H. Beton, *Phys. Rev. X*, 2014, **4**, 011044.

18 M. A. Bissett, S. Konabe, S. Okada, M. Tsuji and H. Ago, *ACS Nano*, 2013, **7**, 10335–10343.

19 F. Hao and X. Chen, *Mater. Res. Express*, 2015, **2**, 105016.

20 H. Li, C. Tsai, A. L. Koh, L. Cai, A. W. Contryman, A. H. Fragapane, J. Zhao, H. S. Han, H. C. Manoharan, F. Abild-Pedersen, J. K. Nørskov and X. Zheng, *Nat. Mater.*, 2016, **15**, 48–53.

21 X. Zhao, Z. Ding, J. Chen, J. Dan, S. M. Poh, W. Fu, S. J. Pennycook, W. Zhou and K. P. Loh, *ACS Nano*, 2018, **12**, 1940–1948.

22 J. Lahiri, Y. Lin, P. Bozkurt, I. I. Oleynik and M. Batzill, *Nat. Nanotechnol.*, 2010, **5**, 326–329.

23 A. Ambrosetti and P. L. Silvestrelli, *J. Phys. Chem. C*, 2017, **121**, 19828–19835.

24 F. Sedona, G. A. Rizzi, S. Agnoli, F. X. Llabres i Xamena, A. Papageorgiou, D. Ostermann, M. Sambi, P. Finetti, K. Schierbaum and G. Granozzi, *J. Phys. Chem. B*, 2005, **109**, 24411–24426.

25 C. Wu, M. S. J. Marshall and M. R. Castell, *J. Phys. Chem. C*, 2011, **115**, 8643–8652.

26 S. Surnev, L. Vitali, M. Ramsey, F. Netzer, G. Kresse and J. Hafner, *Phys. Rev. B*, 2000, **61**, 13945.

27 F. Yang, Y. Choi, P. Liu, D. Stacchiola, J. Hrbek and J. A. Rodriguez, *J. Am. Chem. Soc.*, 2011, **133**, 11474–11477.

28 M. M. Ugeda, I. Brihuega, F. Guinea and J. M. Gómez-Rodríguez, *Phys. Rev. Lett.*, 2010, **104**, 096804.

29 Y. Tison, J. Lagoute, V. Repain, C. Chacon, Y. Girard, F. Joucken, R. Sporken, F. Gargiulo, O. V. Yazyev and S. Rousset, *Nano Lett.*, 2014, **14**, 6382–6386.

30 N. Levy, S. A. Burke, K. L. Meaker, M. Panlasigui, A. Zettl, F. Guinea, A. H. Castro Neto and M. F. Crommie, *Science*, 2010, **329**, 544–547.

31 Y. Liu, J. N. B. Rodrigues, Y. Z. Luo, L. Li, A. Carvalho, M. Yang, E. Laksono, J. Lu, Y. Bao, H. Xu, S. J. R. Tan, Z. Qiu, C. H. Sow, Y. P. Feng, A. H. C. Neto, S. Adam, J. Lu and K. P. Loh, *Nat. Nanotechnol.*, 2018, **13**, 828–834.

32 L. Jones, H. Yang, T. J. Pennycook, M. S. J. Marshall, S. Van Aert, N. D. Browning, M. R. Castell and P. D. Nellist, *Adv. Struct. Chem. Imaging*, 2015, **1**, 8.

33 L. Jones, S. Wang, X. Hu, S. ur Rahman and M. R. Castell, *Adv. Struct. Chem. Imaging*, 2018, **4**, 7.

34 J. P. Perdew and Y. Wang, *Phys. Rev. B*, 1992, **45**, 13244.

35 G. Kresse and D. Joubert, *Phys. Rev. B*, 1999, **59**, 1758.

36 G. Kresse and J. Hafner, *Phys. Rev. B*, 1994, **49**, 14251.

37 G. Kresse and J. Furthmüller, *Phys. Rev. B*, 1996, **54**, 11169.

38 J. Tersoff and D. Hamann, *Phys. Rev. Lett.*, 1983, **50**, 1998.

39 R. F. W. Bader, *Chem. Rev.*, 1991, **91**, 893–928.

40 G. Henkelman, A. Arnaldsson and H. Jónsson, *Comput. Mater. Sci.*, 2006, **36**, 354–360.

41 C. Wu, M. R. Castell, J. Goniakowski and C. Noguera, *Phys. Rev. B*, 2015, **91**, 155424.

42 J. Goniakowski and C. Noguera, *Phys. Rev. B*, 2009, **79**, 155433.

43 J. Goniakowski, C. Noguera, L. Giordano and G. Pacchioni, *Phys. Rev. B*, 2009, **80**, 125403.

44 L. Li, S. Reich and J. Robertson, *Phys. Rev. B*, 2005, **72**, 184109.

45 R. Wang, J. Yang, X. Wu and S. Wang, *Nanoscale*, 2016, **8**, 8210–8219.

46 P. Jacobson, B. Stöger, A. Garhofer, G. S. Parkinson, M. Schmid, R. Caudillo, F. Mittendorfer, J. Redinger and U. Diebold, *J. Phys. Chem. Lett.*, 2012, **3**, 136–139.

47 J. Gao, J. Zhang, H. Liu, Q. Zhang and J. Zhao, *Nanoscale*, 2013, **5**, 9785–9792.

48 J. M. W. Chase, *J. Phys. Chem. Ref. Data*, 1998, **Monograph**, 1–1951.

49 J. D. Cox, D. D. Wagman and V. A. Medvedev, *CODATA Key Values for Thermodynamics*, Hemisphere Publishing Corp., New York, 1984.

50 T. Björkman, S. Kurasch, O. Lehtinen, J. Kotakoski, O. V. Yazyev, A. Srivastava, V. Skakalova, J. H. Smet, U. Kaiser and A. V. Krasheninnikov, *Sci. Rep.*, 2013, **3**, 3482.

51 O. Cretu, A. V. Krasheninnikov, J. A. Rodríguez-Manzo, L. Sun, R. M. Nieminen and F. Banhart, *Phys. Rev. Lett.*, 2010, **105**, 196102.

52 E. Cockayne, G. M. Rutter, N. P. Guisinger, J. N. Crain, P. N. First and J. A. Stroscio, *Phys. Rev. B*, 2011, **83**, 195425.

53 L. Giordano, F. Cinquini and G. Pacchioni, *Phys. Rev. B*, 2006, **73**, 045414.

54 L. Giordano, G. Pacchioni, J. Goniakowski, N. Nilius, E. Rienks and H.-J. Freund, *Phys. Rev. B*, 2007, **76**, 075416.

55 A. Schlapka, M. Lischka, A. Groß, U. Käsberger and P. Jakob, *Phys. Rev. Lett.*, 2003, **91**, 016101.